

Fingering Instability in a Water-Sand Mixture

A. Lange¹, M. Schröter², M. A. Scherer², A. Engel¹, and I. Rehberg²

¹ Institut für Theoretische Physik, Otto-von-Guericke-Universität, Postfach 4120, D-39016 Magdeburg, Germany

² Institut für Experimentelle Physik, Otto-von-Guericke-Universität, Postfach 4120, D-39016 Magdeburg, Germany

The temporal evolution of a water-sand interface driven by gravity is experimentally investigated. By means of a Fourier analysis of the evolving interface the growth rates are determined for the different modes appearing in the developing front. To model the observed behavior we apply the idea of the Rayleigh-Taylor instability for two stratified fluids. Carrying out a linear stability analysis we calculate the growth rates from the corresponding dispersion relations for finite and infinite cell sizes. Taking into account the uncertainty in the viscosity measurements for sand dispersed in water, the theoretical results catch the essence of the experiment but also demonstrate the limitations of this approach.

PACS numbers: 47.54.+r, 47.55.Kf, 68.10.-m, 81.05.Rm, 83.70.Hq

I. INTRODUCTION

There has been great interest in the behavior of granular materials over the last years (for a review see [1] and references therein). Examples for the surprising behavior of granular matter are two-dimensional localized states, called oscillons [2], in vertically vibrated containers, stratification phenomena observed while pouring granular mixtures onto a pile [3] or singing sand audible in deserts [4].

In contrast to the amount of phenomena one lacks a sound theoretical explanation for the observations. Difficulties arise due to the highly complex, disordered structure formed by the grains and their nonlinear internal friction. Therefore, most theoretical approaches have been done by numerical methods. Molecular-dynamics simulations and cellular automata calculations are frequently applied, for recent reviews see, e.g., [5] and [6]. These methods describe in some detail the interactions between the particular grains [7,8]. Conclusions on the macroscopic behavior of granular matter are then drawn from the simulations with a great number of particles. Despite the recent progress in computer performance the size of the systems are still too small for a quantitative comparison with real experiments [7,9].

Hydrodynamic approaches to granular material are few [10–13] and are associated with restrictions as no inter-particle correlations [10], a Gaussian distribution in the velocity of the grains [11] or steady-state properties [13]. Nevertheless, there are striking phenomenological similarities in the observed patterns for pure granular materials and pure fluids. Experiments with an inclined chute [14,15] or a vertically vibrated container [16,17] show the most noticeable analogy. It is clear that granular media are different from fluids but under certain conditions these differences are *not prevailing*.

The flow of grains embedded in an interstitial fluid is dominated either by the effects of grain inertia or by

effects of fluid viscosity. The Bagnold number B [18] expresses the ratio of collision forces between the grains to viscous forces in the fluid-grain mixture. A small Bagnold number, $B < 40$, characterizes the regime of the macro-viscous flow. In this regime the viscous interaction with the pure fluid is important. Examples for this type of flow are mud slides and the transport of water-sand mixtures in river beds. At large Bagnold numbers, $B > 450$, the flow is called grain-inertia regime where the grain-grain interactions dominate. All flows of grains with air as interstitial fluid fall into the grain-grain regime.

Here, experiments are performed with sand dispersed in water. The occurring shear rates, the mean particle diameters, and the viscosity of water result in a low Bagnold number. This motivates the idea to consider the water-sand mixture as fluid-like. In the experiments we observe that the initial flat water-sand interface evolves into a finger-like pattern. To model this behavior we test a continuum approach which is based on a well-known hydrodynamic instability. The aim is to determine the critical parameters for the stability of the pattern and the dispersion relation for the wave numbers detectable in the experiment. To some extend the experiments presented here are similar to those with water and polystyrene spheres performed by Skjeltorp [19]. While Skjeltorp studied the dependence of the initial wavelength of the developing pattern on the width of the cell we focus on the temporal evolution of all wave numbers.

In the following section, the experimental arrangement is described and the results for the growth rates of the wave numbers are presented. In Sec. III the model is explained and thereafter the calculated growth rates are compared with those of the experiment (Sec. IV). The final section contains our conclusions and some remarks about further prospectives.

II. EXPERIMENT

A. Experimental setup

A closed Hele-Shaw-like cell is used to investigate the temporal evolution of a water-sand interface driven by gravity (see Fig. 1). The cell, a CCD-camera and a neon tube are fixed to a frame which can be turned around a horizontal axes. This allows image analysis in the co-moving frame and ensures a homogeneous illumination at every stage of the pattern forming process. The length of the cell is 160 mm, the height 80 mm and the width 4 mm, respectively. The cell is filled with sand and distilled water. As sand we use spherical glass particles (Würth Ballotini MGL) of different sizes and size distributions (see Table I for details). Its material density is given by 2.45 g/cm³. The rotation axes of the frame is right beneath the sand layer. This minimizes the centrifugal forces on the sand layer while the cell is turned. The cell is rotated by hand. To obtain reproducible results the vertical and horizontal acceleration is measured by acceleration sensors (ADXL05). When the cell passes a rotation angle of 170 degree a lightgate triggers a number of snapshots. This moment defines the starting time $t = 0$ of our measurements where we take images every 20 ms for later analysis. The images have a dimension of 256 x 300 pixel. To achieve a reasonable resolution we only focus on a horizontal length of 61 mm at the middle of the cell. This gives a resolution of 4.9 pixel/mm.

B. Experimental results

Fig. 2 shows typical images of the sand-water cell at certain stages. 20 ms after the series of snapshots is started the initial flat sand layer is modulated at small scales (Fig. 2(a)). These disturbances are enhanced and give rise to sand fingers as seen in Fig. 2(c). At later stages the fingers evolve to a mushroom-like pattern (Fig. 2(d) and Fig. 2(e)). This type of pattern was found as well by numerical simulations for two stratified suspensions of different concentration [20].

To analyze this behavior we apply a threshold algorithm to obtain the water-sand interface. We look at every column of our digitized image to determine the point where the grey scale exceeds a certain value. We start at the bottom (water) and continue to the top (sand). In this way we track down the interface of the pattern. Fig. 3 shows the temporal evolution of the images presented in Fig. 2. Here the interfaces of all patterns are shown. While our detecting method works for the patterns during the first stages, namely small scale modulations and sand fingers, it breaks down for mushroom-like patterns. However, this is not crucial because those patterns are beyond the scope of the linear analysis presented here. Discrete-Fourier-Transformation (DFT) gives the Fourier spectrum of each interface. Fig. 4 shows the temporal

evolution of the amplitude A of a typical Fourier mode. It is seen that A grows exponentially from the first taken image to $t = 200$ ms. By an exponential fit

$$A(k) = A_i(k) \exp(n(k)t) \quad (2.1)$$

we obtain the growth rate n for every wave number k in our spectra, where A_i is the initial amplitude.

In order to test the reliability of our experimental setup we perform 100 independent runs with one set of material parameters. The particular values of this set are given in the first row of Table I (Experiment I). We only analyze image series where the angular velocity of our rotating apparatus is larger than 6.6 rad/s. We find that 42 fast runs show only a slight deviation in the angular velocity: 7.4 ± 0.1 rad/s. These 42 measurements are analyzed to obtain a mean growth rate and a mean initial amplitude for each wave number. The results are shown in Fig. 5. It is seen that the growth rates starting with small values increase with increasing wave number until they saturate at larger k . In contrast the initial amplitude decreases for increasing wave numbers. In the case of large wave numbers we do not obtain *exponential* fits for every experimental run. This is due to the fact that the amplitude is very small and that we approach the limit of the resolution of our image processing. The error bars in Fig. 5 indicate that the number of runs which can be analyzed decreases for larger wave numbers.

An obvious question concerning the underlying mechanism of the pattern formation in our system is: How do different material parameters effect the dispersion relation? Therefore we carry out experiments with different material configurations which are characterized in Table I. Using 2 g, 4 g, and 8 g of sand (Experiment I, II, III) we observe a shift of all growth rates towards larger values with increasing mass of sand. This effect is independent of the wave number (Fig. 6 (a)). Using three different size distributions (Experiment I, IV, V) reveals that the mean particle diameter does not have any significant influence on $n(k)$ (Fig. 6 (b)). As a common feature we find the same overall behavior for all material sets: The growth rates increase for small k and reach a plateau for larger values of k .

III. THEORY

We choose a two fluid system as model to describe the experimental results. In the initial state two incompressible fluids of constant densities ρ_1 and ρ_2 and constant dynamical viscosities μ_1 and μ_2 are arranged in two horizontal strata. The index 1 (2) refers to the fluid at the bottom (top) of the system. The pressure is a function of the vertical coordinate z only; x and y are the coordinates in the plane perpendicular to z . The acceleration due to gravity acts in negative z direction. A *linear* stability analysis is carried out for small disturbances of this initial state. The instability of a planar interface

$z = z_s(x, y) \equiv 0$ between the two fluids is known as the Rayleigh-Taylor instability [21,22].

We assume that the boundaries in z direction are far from the interface. Small changes δz_s in the form of the interface cause a pressure difference which is balanced by the product of the surface tension T_s and the curvature of the interface. Considering small disturbances $\delta\rho$ in the density and δp in the pressure the Navier-Stokes equations read [22]

$$\rho\partial_t u = -\partial_x \delta p + \mu\Delta u + (\partial_x w + \partial_z u)\partial_z \mu \quad , \quad (3.1)$$

$$\rho\partial_t v = -\partial_y \delta p + \mu\Delta v + (\partial_y w + \partial_z v)\partial_z \mu \quad , \quad (3.2)$$

$$\begin{aligned} \rho\partial_t w &= -\partial_z \delta p + \mu\Delta w + 2\partial_z w\partial_z \mu - g\delta\rho \\ &+ T_s(\partial_x^2 + \partial_y^2)\delta z_s\delta(z - z_s) \quad , \end{aligned} \quad (3.3)$$

where $\partial_i = \partial/\partial i$, $i = x, y, z, t$. The z dependence of μ gives rise to the third term at the right-hand side of (3.1-3.3) since the viscous part in the Navier-Stokes equations is $\partial_j[\mu(\partial_j v_i + \partial_i v_j)]$ for an incompressible fluid. For convenience, we adhere to $\partial_z \mu$ though $\partial_z \mu$ is different from zero only at the interface. The components of the velocity field \vec{v} are $v_x = u$, $v_y = v$, and $v_z = w$ and are considered as small, so Eqs. (3.1-3.3) contain only terms which are linear in the disturbances. The delta-function $\delta(z - z_s)$ ensures that the surface tension appears at the interface z_s between the two fluids. The equation of continuity (mass conservation) for an incompressible fluid is

$$\operatorname{div} \vec{v} = \partial_x u + \partial_y v + \partial_z w = 0 \quad . \quad (3.4)$$

Additionally the equation

$$\partial_t \delta\rho = -(\vec{v} \operatorname{grad})\rho = -w\partial_z \rho \quad (3.5)$$

relates the temporal variations in the density fluctuations to the density jump at the interface which moves with w in z direction. The Eqs. (3.1-3.5) govern the linearized system. The disturbances are analyzed into *normal modes* thus seeking solutions which x and t dependence is proportional to $\exp(ikx + nt)$. The wave number is denoted by k and $n(k)$ is the growth rate of the corresponding mode k . If the fluid is confined between two rigid planes the boundary conditions are

$$w = \partial_z w = 0 \quad \text{at } z = \pm\infty \quad . \quad (3.6)$$

where we shift the planes to infinity for the sake of simplicity. The other boundary conditions are related to the interface. All three components of the velocity and the tangential viscous stresses must be continuous. Using the exponential ansatz for the continuous velocity components, Eq. (3.4) gives the continuity of $\partial_z w$, too. The continuity of $\mu(\partial_z^2 + k^2)w$ is the condition which ensures that the two tangential stress components are continuous across the interface. Inserting the exponential ansatz into (3.1-3.5) and eliminating δp leads to

$$\begin{aligned} \partial_z \left\{ \left[\rho - \frac{\mu}{n}(\partial_z^2 - k^2) \right] \partial_z w - \frac{1}{n} \partial_z \mu (\partial_z^2 + k^2) w \right\} &= \\ k^2 \left\{ \left[-\frac{g}{n^2} \partial_z \rho + \frac{k^2}{n^2} T_s \delta(z - z_s) \right] w \right. \\ \left. + \left[\rho - \frac{\mu}{n}(\partial_z^2 - k^2) \right] w - \frac{2}{n} \partial_z \mu \partial_z w \right\} \quad . \end{aligned} \quad (3.7)$$

For each region ρ and μ are considered as constant which reduces Eq. (3.7) to

$$\left[1 - \frac{\nu_{1,2}}{n}(\partial_z^2 - k^2) \right] (\partial_z^2 - k^2) w = 0 \quad . \quad (3.8)$$

The appropriate solution of (3.8) is

$$w_1 = A_1 e^{+kz} + B_1 e^{+q_1 z} \quad \text{for } z \leq 0 \quad , \quad (3.9)$$

$$w_2 = A_2 e^{-kz} + B_2 e^{-q_2 z} \quad \text{for } z \geq 0 \quad , \quad (3.10)$$

which satisfies the boundary condition (3.6). We introduced $q_{1,2}^2 = k^2 + n/\nu_{1,2}$ where $\nu_{1,2} = \mu_{1,2}/\rho_{1,2}$ is the kinematic viscosity for each region. In (3.9, 3.10) only the positive real part of $q_{1,2}$ is accepted.

The dispersion relation follows from the analysis at the interface. The continuity of w , $\partial_z w$, and $\mu(\partial_z^2 + k^2)w$ at $z_s = 0$ provides three equations to determine the four constants in (3.9, 3.10). The forth equation is given by integrating (3.7) across the interface and then taking the limit that the integration interval goes to zero. The condition for a nontrivial solution yields the dispersion relation [22]

$$\begin{aligned} &-\left\{ \frac{gk}{n^2} \left[(\alpha_1 - \alpha_2) + \frac{k^2 T}{g(\rho_1 + \rho_2)} \right] + 1 \right\} (\alpha_2 q_1 + \alpha_1 q_2 - k) \\ &- 4k\alpha_1\alpha_2 + \frac{4k^2}{n} (\alpha_1\nu_1 - \alpha_2\nu_2) [\alpha_2 q_1 - \alpha_1 q_2 + k(\alpha_1 - \alpha_2)] + \frac{4k^3}{n^2} (\alpha_1\nu_1 - \alpha_2\nu_2)^2 (q_1 - k)(q_2 - k) = 0, \end{aligned} \quad (3.11)$$

with $\alpha_{1,2} = \rho_{1,2}/(\rho_1 + \rho_2)$. For the rest of the paper we will use a dimensionless surface tension $S = T/[(\rho_1 + \rho_2)(g\nu_1^4)^{1/3}]$ if not stated otherwise.

We now briefly discuss the general results of the dispersion relation (3.11). The configuration where the lighter fluid is on top of the heavier one, $\rho_2 < \rho_1$, is always stable, i.e., $\operatorname{Re}\{n(k)\} \leq 0$ for all k . This is independent of whether there is any surface tension (Fig. 7 (b)) or not (Fig. 7 (a)). If the strata are in the opposite order, $\rho_2 > \rho_1$, then the surface tension plays a crucial role. In the case of no surface tension (Fig. 8 (a)) the system is unstable against disturbances of any wave number, i.e., $\operatorname{Re}\{n(k)\} \geq 0$ for all k . If there is a surface tension a critical wave number exists

$$k_c = \sqrt{\frac{g}{T}(\rho_2 - \rho_1)} \quad , \quad (3.12)$$

and the system is stable (unstable) against modes with wave numbers which are larger (smaller) than k_c (Fig. 8

(b)). A moderate variation in the relation between the two viscosities ν_1 and ν_2 has no strong influence on the general behavior of the growth rates (see Figs. 7 and 8).

The experiments are carried out in a finite-size cell in contrast to our simplification of infinite length in z direction. We determine now the limits to which this simplification is justified (see also [23]). If the walls of the cell are at $z = \pm L_z$ the ansatz (3.9-3.10) modifies to

$$w_1 = a_1 e^{+kz} + a_2 e^{-kz} + b_1 e^{+q_1 z} + b_2 e^{-q_1 z} \quad \text{for } z \leq 0, \quad (3.13)$$

$$w_2 = c_1 e^{+kz} + c_2 e^{-kz} + d_1 e^{+q_1 z} + d_2 e^{-q_1 z} \quad \text{for } z \geq 0. \quad (3.14)$$

With the boundary condition $w = \partial_z w = 0$ at $z = \pm L_z$ and the analysis at the interface as above one ends up with a system of eight equations for the constants in (3.13-3.14). The coefficients of the corresponding matrix are given in the Appendix. The vanishing determinant leads to the dispersion relation $n(k)$, its numerical solution is shown in Fig. 9 for different lengths L_z . The comparison with the data for infinite L_z shows that there is no real difference as long as $|L_z| > 3$ mm for the used material parameters. Since the thickness of the sand layer is below this margin we expect finite-size effects. In the case of asymmetrical arranged walls at $z = -L_1$ and $z = +L_2$ the dispersion relation shows up to a ratio of $|L_1|/L_2 \simeq 17$ only a very weak deviation from the results for symmetrical walls.

In the frame of our continuum approach we consider the water-sand mixture as a suspension in accordance with the classification in [24]. The dispersion medium is water and the dispersed material consists of sand particles with a mean diameter and a density as stated in Sec. II. The material density as well as the dynamical viscosity of the mixture depend on the packing density ϕ of the granular material. The packing density ϕ measures the volumetric concentration of the particles in the mixture. In the concept of a 'simple mixture' the material density of the mixture is given by [25]

$$\rho_{mixture} = \phi \rho_{sand} + (1 - \phi) \rho_{water} . \quad (3.15)$$

In the following the index 1 refers to water and 2 to the mixture, respectively. Two empirical formulae [26,27]

$$\frac{\mu_2}{\mu_1} = \mu_r = \left(1 - \frac{\phi}{\phi_{max}}\right)^{-2.5\phi_{max}} \quad \phi_{max} = 0.63, \quad (3.16)$$

$$\frac{\mu_2}{\mu_1} = \mu_r = \left(1 + \frac{0.75}{\frac{\phi_{max}}{\phi} - 1}\right)^2 \quad \phi_{max} = 0.605, \quad (3.17)$$

were used for the dynamical viscosity of a hard sphere suspension. The maximal packing densities in (3.16, 3.17) result from the fit of the proposed formulae with the experimental results. These empirical formulae were validated in recent measurements for colloidal systems [28,29] with particle diameters between 155 and 640 nm

and for clay-water suspensions with mean particle diameters of few micrometers [30].

Figure 10 shows the behavior of the relative dynamical viscosity μ_r for different packing densities ϕ according to Eqs. (3.16, 3.17). A third relation, $\mu_r \simeq 1/[1 - (\phi/\phi_{max})]^{1/3}$ with $\phi_{max} = 0.625$, was also plotted where particle sizes beyond the colloidal range were incorporated into the theoretical basis of this relation [31]. All three of them give nearly the same value for $\mu_r(\phi)$ at moderately dense packings, $0.4 \leq \phi \leq 0.48$. Above this region the relative viscosity diverges as ϕ approaches its maximal value. But the strength of the divergent behavior is remarkable different so that μ_r already varies about a factor of 5 for $\phi = 0.57$. An interpretation of this fact could be that only when ϕ is *very close* to ϕ_{max} that then the different particle diameters and their fraction in the suspension play a distinctive role.

IV. RESULTS AND DISCUSSION

In experiment I the height measurements for the sand layer in the cell result in a value of $\phi = 0.48$. Thus the mixture is sufficiently characterized by Eqs. (3.15-3.17) where $\rho_{water} = 0.988 \text{ g/cm}^3$. By means of (3.17) the viscosity of the mixture is $\mu_2 \simeq 15\mu_1$ for $\phi = 0.48$. The resulting growth rates are entirely misleading for infinite L_z as well as for finite L_z (Fig. 11). Since the relative dynamical viscosity is the most uncertain quantity in our calculations we consider μ_r now as a quasi free parameter to find the best fit with the experimental data. Under the assumption of zero surface tension a least square fit results in $\mu_2 \simeq 104\mu_1$ which gives a fairly good agreement over the whole k range. In comparison to $\mu_2 \simeq 104\mu_1$ fits with $\mu_2 \simeq 128\mu_1$ and $\mu_2 \simeq 85\mu_1$ show a better agreement for smaller and larger wave numbers k , respectively.

For two sets of parameters, $\mu_2 \simeq 15\mu_1$ and $\mu_2 \simeq 104\mu_1$, we calculate the dispersion relation for infinite as well as for finite L_z . The finite-size effects appear for small wave numbers and diminish with increasing wave numbers. The differences in $n(k)$ for small wave numbers are more pronounced for larger relative viscosities (see Fig. 11). The dispersion relations for infinite and finite L_z approach each other at wave numbers where the initial amplitudes of the disturbances are in the order of 10^{-2} mm. For these disturbances a boundary at 2.6 mm distance appears to be at infinity. Therefore it does not matter whether we choose $L_z = \pm\infty$ or $L_z = \pm 2.6$ mm. This is not the case for small wave numbers where the initial amplitudes are in the order of 10^{-1} mm (Fig. 5 (b)).

There is one viscosity measurement [32] which comes near to the value of the relative viscosity suggested by our fit. The measurement was carried out for crushed sand with particle diameters from 20 to 80 μm and gives a value of $\mu_2 \sim 110\mu_1$ for $\phi = 0.48$ (see Fig. 3 in [32]). This value for the relative viscosity is noteable close to

our fit value. Nevertheless, the large difference in μ_r between [26,27,31] and [32] over a wide range of the packing density ϕ represent an unsatisfying situation. It highlights the need for comprehensive and unambiguous viscosity measurements in highly concentrated hard sphere suspensions. Furthermore, it shows how sensitive μ_r is on experimental methodes [31].

The aspect ratio of the cell suggests that a description referring to the Hele-Shaw type of the cell might be closer to the experimental configuration. Adapting the dispersion relation of the Saffman-Taylor instability to the case of zero throughflow velocity leads to (see [33], Eq. (10))

$$n(k) = \frac{b^2}{12(\mu_1 + \mu_2)} [kg(\rho_2 - \rho_1) - Tk^3] \quad (4.1)$$

where $b = 4$ mm denotes the width of the cell. In contrast to the Rayleigh-Taylor approach Eq. (4.1) contains two parameters, the dynamical viscosity μ_2 of the mixture and the surface tension T , which have to be determined by a least square fit. The validity of the Hele-Shaw approach is limited by a cut-off condition at which the wave number exceeds $2\pi/b$.

The fit values $\mu_2 \simeq 404 \mu_1$ and $T \simeq 1.06 \cdot 10^{-3} \text{ Nm}^{-1}$ result in a fit curve which is inferior to the Rayleigh-Taylor fit (Fig. 12). Additionally, both fit parameters are questionable. The value $\mu_2 \simeq 404 \mu_1$ is beyond any realistic one for the dynamical viscosity of the mixture at a packing density of $\phi = 0.48$. A nonzero surface tension between the water-sand mixture and water is as well arguable.

The better agreement of the Rayleigh-Taylor approach with the experimental data is backed up by calculations focused on the influence of finite cell boundaries for Rayleigh-Bénard convection [34]. As long as the ratio between the relevant height of the cell and its width is smaller than 0.8, the assumption of infinite boundaries in y direction is a good approximation. If this ratio is larger than 5 the Hele-Shaw approach is well-founded. The height of the sand layer and the width of the cell give a ratio of 0.65 which supports the Rayleigh-Taylor approach.

It has to be stressed that both the Hele-Shaw and the Rayleigh-Taylor approach assume a trivial y dependence of the flow. In the experiment, that assumption is not satisfied: The rotation of the apparatus leads to a sand layer which is not perfectly flat even in the beginning of the flow process. The strength of this effect is presently hard to determine, however.

V. CONCLUDING REMARKS

In a closed Hele-Shaw-like cell the temporal evolution of a water-sand interface was investigated. For the instable stratification, sand above water, the instability is driven by gravity. The images of the temporal evolution were analyzed by DFT. The Fourier spectra show that

the initial disturbances of the interface grow exponentially at the beginning of the pattern forming process. This enables us to determine the growth rates by an exponential fit for every wave number in our spectra. The data show that the growth rate increases with increasing wave number until it saturates at larger values of k . This general behavior is not influenced by the mean particle diameter which was tested with three different size distributions. Experiments with different amounts of sand reveal a shift of the dispersion relation $n(k)$ as a whole. By increasing the mass of sand $n(k)$ is shifted towards larger values of n .

To describe the general behavior we choose a two-fluid system as a model. Carrying out a linear stability analysis for the interface between the two fluids we calculate the growth rates from the dispersion relation for a finite-size cell. The theoretical results agree with the essence in the experimental findings when assuming a relative viscosity of the water-sand mixture which is close to one measured with crushed sand and water [32].

Considering our simplifications and the uncertainty in one relevant material parameter the continuum approach gives a reasonable agreement with the experimental results. This confirms a certain analogy between concentrated suspensions and fluids which was found also in numerical simulations [20]. However, further investigations need to be done in order to clarify open questions.

The available experimental data give no hint on whether the dispersion relation $n(k)$ will have a second zero at k_c after the observed plateau. This would mean a non-zero interfacial tension according to (3.12). It is known [35,36] that an interfacial tension modulates the displacement of the boundary layer under high concentration gradients. Such a concentration gradient concerning sand is present in our system between the water and the water-sand layer. By reducing the density difference between the layers, measurements for k values beyond the plateau should be possible. This can lead towards the determination of k_c and the interfacial tension, respectively.

Since a linear stability analysis is restricted to terms linear in the disturbances we can not take into account fluctuations in the relative viscosity of the mixture. These would lead to terms of higher order because all terms which contain the viscosity are already linear in the velocity disturbances (see 3.1-3.3). On the other side, considering fluctuations of $\rho_{mixture}(\phi)$, i.e., fluctuations of the packing density ϕ implies variations of $\mu_r(\phi)$. This given inconsistency owing to the restrictions of our linear theory can only be resolved in a nonlinear analysis.

VI. ACKNOWLEDGEMENTS

We are grateful to Lluis Carillo, Stefan Neser, and Stefan Schwarzer for inspiring discussions. The experiments were supported by DFG through Re 588/11-1.

VII. APPENDIX

The matrix elements for finite L_z are $A_{11} = e^{-kL_z}$, $A_{12} = e^{kL_z}$, $A_{13} = e^{-q_1L_z}$, $A_{14} = e^{q_1L_z}$, $A_{15} = A_{16} = A_{17} = A_{18} = 0$, $A_{21} = ke^{-kL_z}$, $A_{22} = -ke^{kL_z}$, $A_{23} = q_1e^{-q_1L_z}$, $A_{24} = -q_1e^{q_1L_z}$, $A_{25} = A_{26} = A_{27} = A_{28} = A_{31} = A_{32} = A_{33} = A_{34} = 0$, $A_{35} = e^{kL_z}$, $A_{36} = e^{-kL_z}$, $A_{37} = e^{q_2L_z}$, $A_{38} = e^{-q_2L_z}$, $A_{41} = A_{42} = A_{43} = A_{44} = 0$, $A_{45} = ke^{kL_z}$, $A_{46} = -ke^{-kL_z}$, $A_{47} = q_2e^{q_2L_z}$, $A_{48} = -q_2e^{-q_2L_z}$, $A_{51} = A_{52} = A_{53} = A_{54} = 1$, $A_{55} = A_{56} = A_{57} = A_{58} = -1$, $A_{61} = k$, $A_{62} = -k$, $A_{63} = q_1$, $A_{64} = -q_1$, $A_{65} = -k$, $A_{66} = k$, $A_{67} = -q_2$, $A_{68} = q_2$, $A_{71} = A_{72} = 2\mu_1k^2$, $A_{73} = A_{74} = \mu_1(q_1^2 + k^2)$, $A_{75} = A_{76} = -2\mu_2k^2$, $A_{77} = A_{78} = -\mu_2(q_1^2 + k^2)$, $A_{81} = R/2 - C - \alpha_1$, $A_{82} = R/2 + C + \alpha_1$, $A_{83} = R/2 - q_1C/k$, $A_{84} = R/2 + q_1C/k$, $A_{85} = R/2 - C + \alpha_2$, $A_{86} = R/2 + C - \alpha_2$, $A_{87} = R/2 - q_2C/k$, and $A_{88} = R/2 + q_2C/k$. Furthermore, the abbreviations

$$R = \frac{k}{n^2} \left[g(\alpha_2 - \alpha_1) + \frac{k^2 T}{\rho_1 + \rho_2} \right] \quad \text{and} \quad (7.1)$$

$$C = \frac{k^2}{n} (\alpha_1 \nu_1 - \alpha_2 \nu_2) \quad (7.2)$$

were used.

-
- [1] H. M. Jaeger, S. R. Nagel, and R. P. Behringer, *Rev. Mod. Phys.* **68**, 1259 (1996).
 - [2] P. B. Umbanhowar, F. Melo, and H. L. Swinney, *Nature* **382**, 793 (1996).
 - [3] H. A. Makse, S. Havlin, P. R. King, and H. E. Stanley, *Nature* **386**, 379 (1997).
 - [4] D. E. Goldsack, M. F. Leach, and C. Kilkenny, *Nature* **386**, 29 (1997).
 - [5] G. H. Ristow, in *Annual Reviews of Computational Physics*, Vol. I, edited by D. Stauffer (World Scientific, Singapore, 1994), p. 275.
 - [6] S. Vollmar and H. Herrmann, *Physica A* **215**, 411 (1995).
 - [7] V. Buchholtz, T. Pöschel, and H.-J. Tielmans, *Physica A* **216**, 199 (1995).
 - [8] T. Pöschel and V. Buchholtz, *J. Phys. I (France)* **5**, 1431 (1995).
 - [9] G. A. Kohring, *J. Phys. I (France)* **5**, 1551 (1995).
 - [10] P. K. Haff, *J. Fluid Mech.* **134**, 401 (1983); J. T. Jenkins and M. W. Richman, *J. Fluid Mech.* **192**, 313 (1988).
 - [11] J. T. Jenkins and S. B. Savage, *J. Fluid Mech.* **130**, 187 (1983); J. T. Jenkins, *J. Appl. Mech.* **59**, 120 (1992).
 - [12] H. Hayakawa, S. Yue, and D. C. Hong, *Phys. Rev. Lett.* **75**, 2328 (1995).
 - [13] E. L. Grossman, T. Zhou, and E. Ben-Naim, *Phys. Rev. E* **55**, 4200 (1997).
 - [14] O. Pouliquen, J. Delour, and S. B. Savage, *Nature* **386**, 816 (1997); O. Pouliquen and S. B. Savage, *Fingering instability in granular chute flows*, preprint (1996).

- [15] H. E. Huppert, *Nature* **300**, 427 (1982).
- [16] F. Melo, P. Umbanhowar, and H. L. Swinney, *Phys. Rev. Lett.* **72**, 172 (1994).
- [17] S. Fauve, K. Kumar, C. Laroche, D. Beysens, and Y. Garrabos, *Phys. Rev. Lett.* **68**, 3160 (1992).
- [18] R. A. Bagnold, *Proc. R. Soc. London A* **225**, 49 (1954); **295**, 219 (1966).
- [19] A. T. Skjeltorp, in *Time-Dependent Effects in Disordered Materials*, edited by R. Pynn and T. Riste (Plenum Press Corporation, New York, 1987), p. 71.
- [20] O. A. Druzhinin, *Phys. Fluids* **7**, 315 (1997).
- [21] Lord Rayleigh, *Proc. London Math. Soc.* **14**, 170 (1883); G. Taylor, *Proc. R. Soc. London A* **201**, 192 (1950); D. J. Lewis, *Proc. R. Soc. London A* **202**, 81 (1950).
- [22] S. Chandrasekhar, *Hydrodynamic and Hydromagnetic Stability* (Oxford University Press, Oxford, 1961), Chapt. X.
- [23] K. O. Mikaelian, *Phys. Rev. E* **54**, 3676 (1996).
- [24] H. Rumpf, *Particle Technology* (Chapman and Hall, London, 1990), p. 8.
- [25] D. D. Joseph and Y. Y. Renardy, *Fundamentals of Two-Fluid Dynamics* (Springer Verlag, New York, 1993), Chapt. X.
- [26] I. M. Krieger and T. J. Dougherty, *Trans. Soc. Rheol.* **3**, 137 (1959).
- [27] J. S. Chong, E. B. Christiansen, and A. D. Baer, *J. Appl. Polym. Sci.* **15**, 2007 (1971).
- [28] C. G. de Kruif, E. M. F. van Iersel, and A. Vrij, *J. Chem. Phys.* **83**, 4717 (1985).
- [29] S.-E. Phan, W. B. Russel, Z. Cheng, J. Zhu, P. M. Chaikin, J. H. Dunsmuir, and R. H. Ottewill, *Phys. Rev. E* **54**, 6633 (1996).
- [30] P. Coussot, *Phys. Rev. Lett.* **74**, 3971 (1995).
- [31] N. A. Frankel and A. Acrivos, *Chem. Eng. Sci.* **22**, 169 (1967); A. Acrivos in *Particulate Two-Phase Flow*, edited by M. C. Rocco (Butterworth-Heinemann, Boston, 1993), p. 169.
- [32] L. Arnaud and C. Boutin, in *Theoretical and Applied Rheology*, edited by P. Moldenaers and R. Keunings (Elsevier, Amsterdam, 1992), p. 640.
- [33] P. G. Saffman and G. Taylor, *Proc. R. Soc. London A* **245**, 312 (1958).
- [34] H. Frick and R. M. Clever, *ZAMP* **31**, 502 (1980).
- [35] M.-Q. López-Salvans, P. P. Trigueros, S. Vallmitjana, J. Claret, and F. Sagués, *Phys. Rev. Lett.* **76**, 4062 (1996).
- [36] M. Ronay, *J. Colloid Interface Sci.* **66**, 55 (1978).

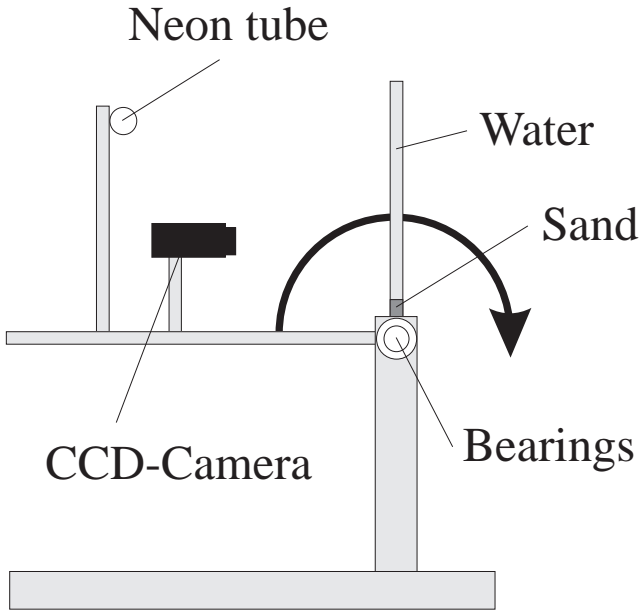


FIG. 1. Experimental setup.

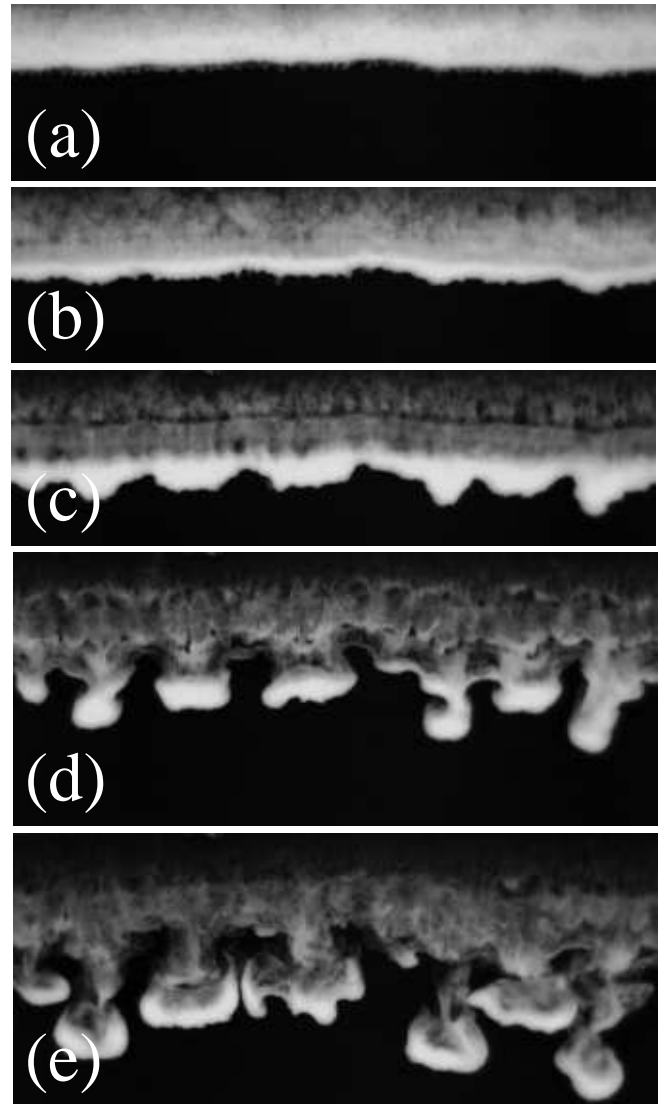


FIG. 2. Sand-water interfaces at certain time steps: (a) 20 ms, (b) 80 ms, (c) 140 ms, (d) 200 ms, and (e) 260 ms. The size distribution of the sand particles is given by $71\text{-}80 \mu\text{m}$ and the sand mass in the cell by 2 g, respectively. The presented frames show the middle part of the cell and have a horizontal length of 68 mm.

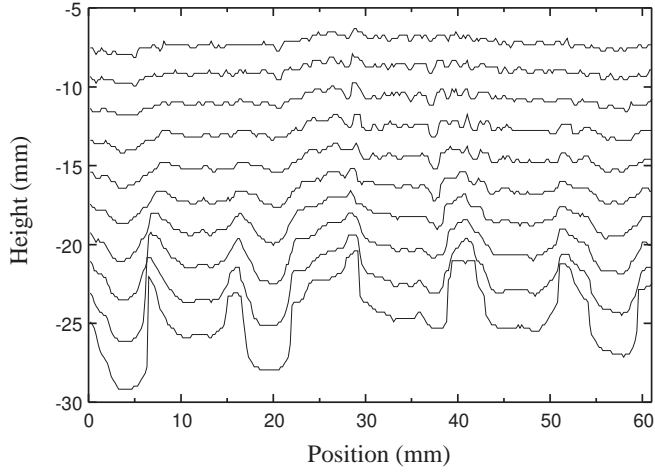


FIG. 3. Temporal evolution of the water-sand interfaces. The patterns are detected every 20 ms and shown with a constant vertical offset of 1 mm. The experimental conditions are the same as in Fig. 2.

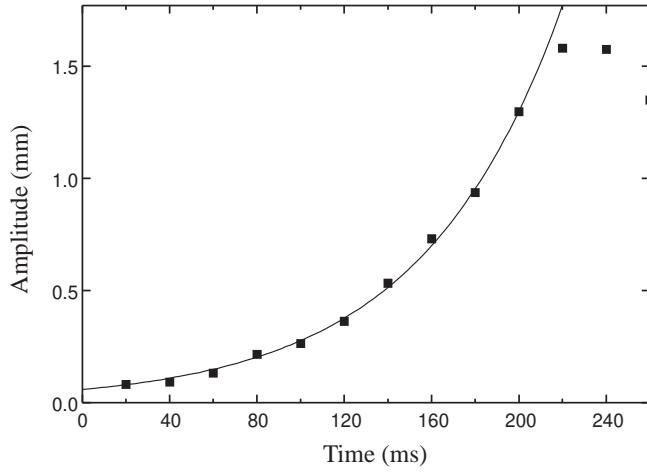


FIG. 4. Amplitude A of a DFT-analysis for a typical wavenumber (here $k = 7 \text{ cm}^{-1}$) in dependence on time t . An exponential fit is obtained by Eq. (2.1). The values belong to the interfaces presented in Fig. 3.

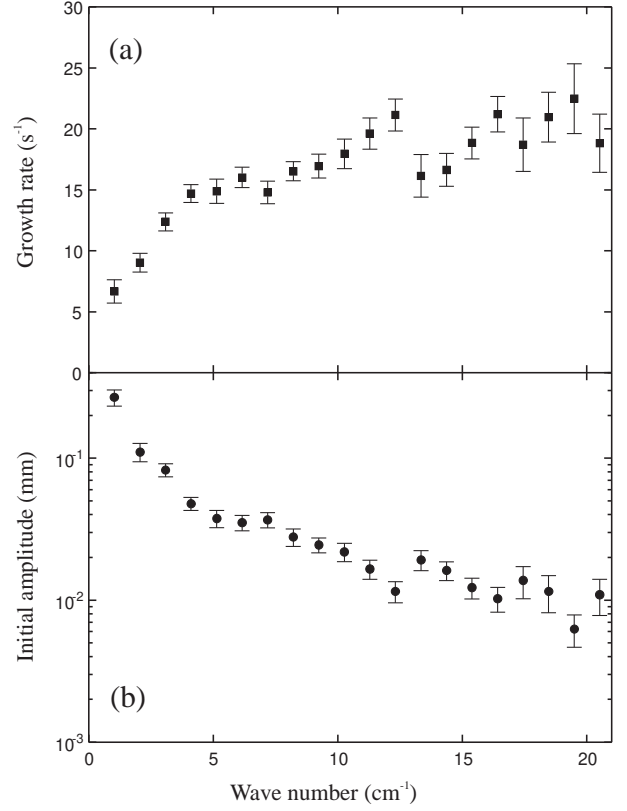


FIG. 5. Growth rate (a) and initial amplitude (b) versus the wavenumber k for experiment I (see Table I).

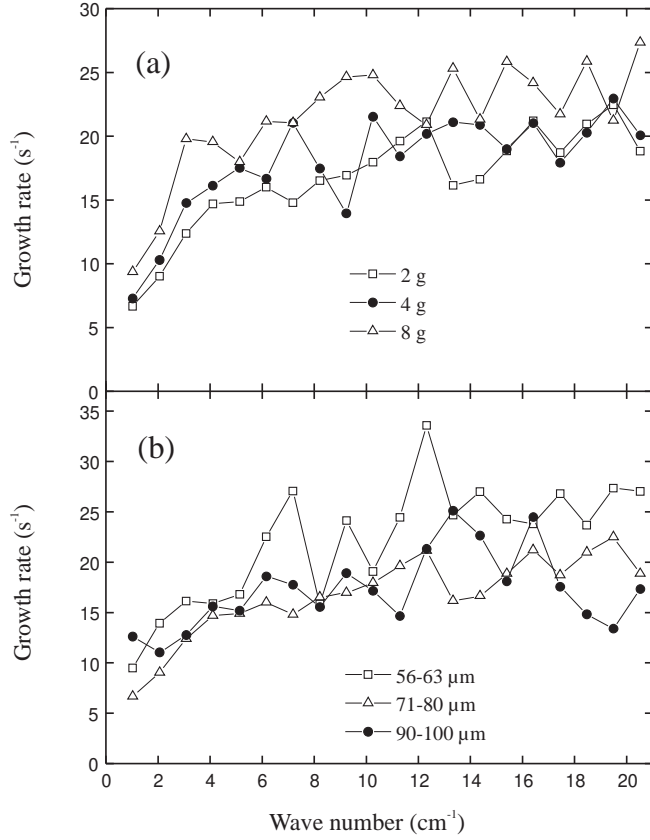


FIG. 6. Growth rate versus the wave number for different material parameters. In (a) 2 g (\square), 4 g (\bullet), and 8 g (\triangle) of sand with the same size distribution were used (Experiment I, II, III). In (b) 2 g of sand with size distributions of 56 – 63 μm (\square), 71 – 80 μm (\triangle), and 90 – 100 μm (\bullet) were used (Experiment IV, I, V).

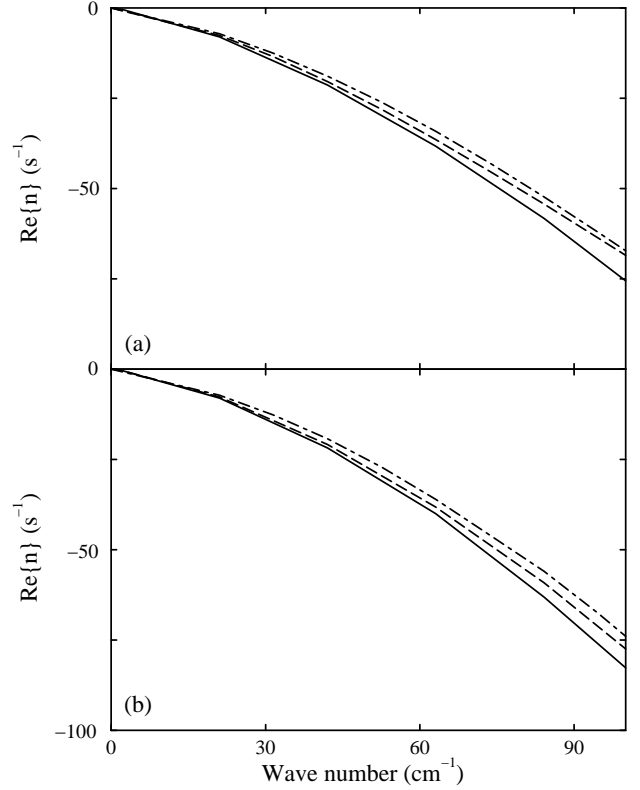


FIG. 7. For zero surface tension (a) and surface tension $S = 1$ (b) the growth rate $\text{Re}\{n\}$ of the modes is plotted versus their wave number k for the case that the top fluid is lighter than the bottom one, $\rho_2 = 0.5\rho_1$. The surface tension as well as the relation of the viscosities does not change the *overall* behavior too much as the three examples show: $\nu_1 = \nu_2 = 10^{-6} \text{ m}^2 \text{ s}^{-1}$ (solid line), $\nu_1 = 10^{-6} \text{ m}^2 \text{ s}^{-1}$ and $\nu_2 = 0.75\nu_1$ (long-dashed line), and $\nu_2 = 10^{-6} \text{ m}^2 \text{ s}^{-1}$ and $\nu_1 = 0.75\nu_2$ (dot-dashed line).

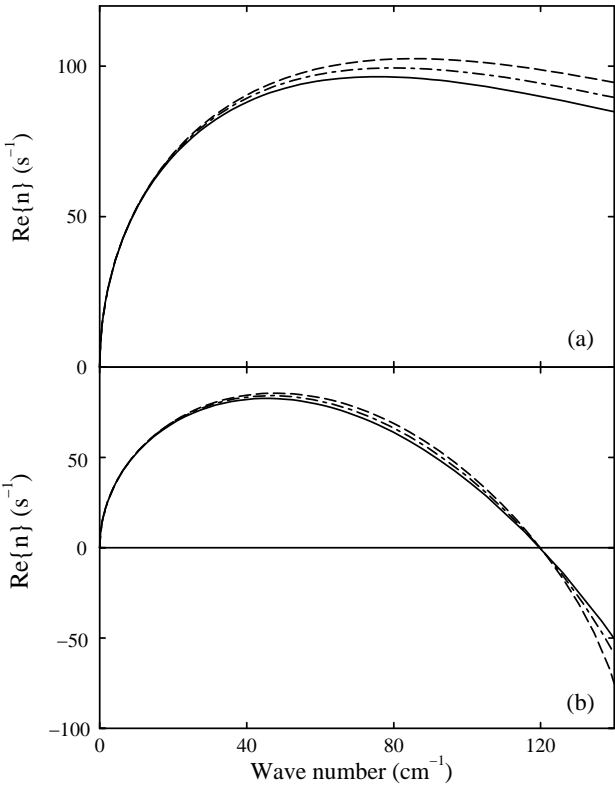


FIG. 8. The growth rate $\text{Re}\{n\}$ of the modes is plotted versus their wave number k for the case that the top fluid is heavier than the bottom one, $\rho_2 = 2\rho_1$. The surface tension S is zero in (a) and 1 in (b). The surface tension causes a drastic change in the behavior whereas the ratio of the viscosities does not change the *overall* behavior too much as the three examples show: $\nu_1 = \nu_2 = 10^{-6} \text{ m}^2 \text{ s}^{-1}$ (solid line), $\nu_1 = 10^{-6} \text{ m}^2 \text{ s}^{-1}$ and $\nu_2 = 0.75\nu_1$ (long-dashed line), and $\nu_2 = 10^{-6} \text{ m}^2 \text{ s}^{-1}$ and $\nu_1 = 0.75\nu_2$ (dot-dashed line).

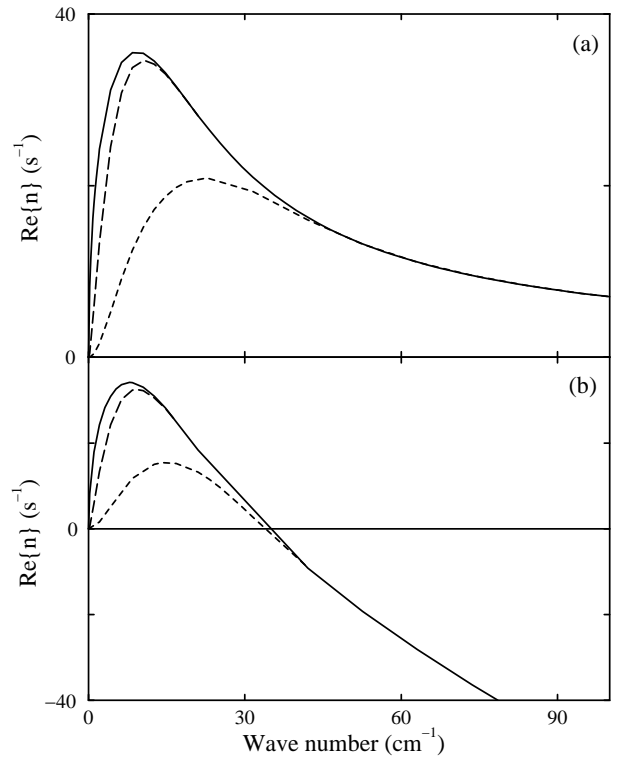


FIG. 9. For zero surface tension (a) and surface tension $S = 12.8$ (b) the growth rate $\text{Re}\{n\}$ is plotted versus the wave number k for $L_z = \pm 3 \text{ mm}$ (long-dashed line) and $L_z = \pm 1 \text{ mm}$ (dashed line). For comparison the solid line shows the graph for infinite L_z . It reveals that finite-size effects play a significant role if $k < 2\pi/|L_z|$. The material parameters are $\rho_2 = 2\rho_1$ and $\nu_2 = 33\nu_1$ with $\rho_1 = 1 \text{ g cm}^{-3}$ and $\nu_1 = 10^{-6} \text{ m}^2 \text{ s}^{-1}$.

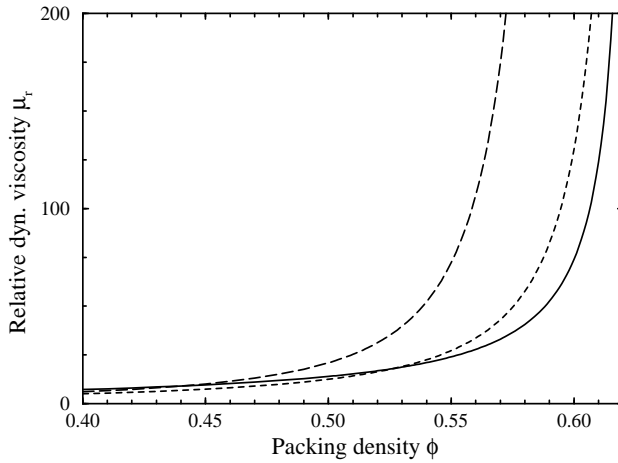


FIG. 10. Relative dynamical viscosity μ_r versus the packing density ϕ . The results of the two empirical formulae (3.16, 3.17) are plotted as dashed and long-dashed lines, respectively. The solid line indicates $\mu_r \simeq 1/ [1 - (\phi/\phi_{max})]^{1/3}$ with $\phi_{max} = 0.625$ [31]. μ_r is nearly the same for all three approaches provided the packing is not too dense, $\phi \leq 0.48$. Above this range μ_r starts to diverge as ϕ reaches ϕ_{max} where the divergent behavior differs significantly between the various approximations.

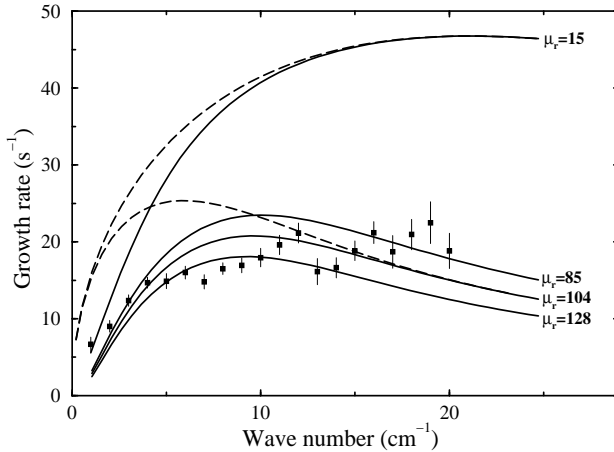


FIG. 11. Growth rates n of the disturbances against their wave numbers k for a packing density $\phi = 0.48$. The results $n(k)$ for infinite L_z according to (3.11) are shown by the dashed line ($\mu_r = 15$) and the long-dashed line ($\mu_r = 104$), respectively. The solid lines are calculated with $|L_z| = \pm 2.6$ mm, the measured height of the sand layer. The relative viscosity for each drawn curve is stated at the right end of it. The finite-size effects appear for small wave numbers and increase with increasing relative viscosity. A relative viscosity of $\mu_r = 15$ based on (3.17) gives growth rates which are far away from the experimental results (■). The best fit over the whole k range gives $\mu_r = 104$. Fits with slightly smaller or larger μ_r values deliver better agreements either with larger or smaller wave numbers.

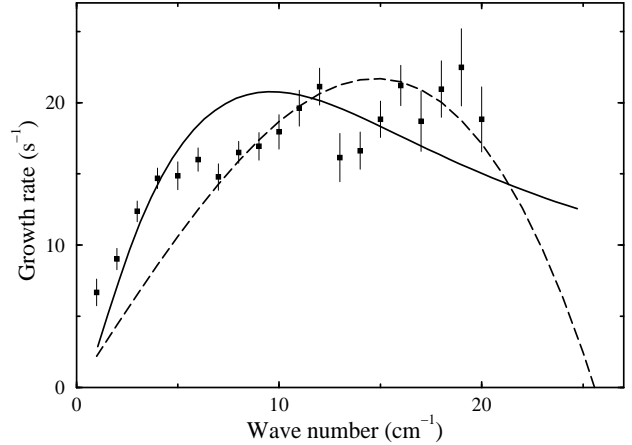


FIG. 12. Growth rates n of the disturbances against their wave numbers k for a packing density $\phi = 0.48$. Two different fits are compared with the experimental results (■). The solid line shows the graph based on the Rayleigh-Taylor approach with finite z boundaries at $|L_z| = \pm 2.6$ mm and $\mu_r = 104$. The long-dashed line presents the results of the Hele-Shaw approach with $\mu_r = 404$ and $T \simeq 1.06 \cdot 10^{-3}$ Nm⁻¹.

TABLE I. Details of sand used in certain experimental configurations.

Experiment	Size distribution [μm]	Mass [g]	Runs
I	71-80	2	100
II	71-80	4	12
III	71-80	8	12
IV	56-63	2	12
V	90-100	2	12